

Efficient Photocatalytic Hydrogen Peroxide Generation Coupled with Selective Benzylamine Oxidation over Defective ZrS₃ Nanobelts

Zhangliu Tian

National University of Singapore

Cheng Han

Shenzhen University

Yao Zhao

National University of Singapore

Weirui Dai

National University of Singapore

Xu Lian

National University of Singapore

Yanan Wang

Department of Physics, National University of Singapore, Singapore 117542

Yue Zheng

National University of Singapore

Yi Shi

National University of Singapore

Xuan Pan

National University of Singapore

Zhichao Huang

National University of Singapore

Hexing Li

Shanghai Normal University

Wei Chen (✉ phycw@nus.edu.sg)

Department of Physics, National University of Singapore, Singapore 117551, Singapore

<https://orcid.org/0000-0002-1131-3585>

Article

Keywords: Photocatalytic hydrogen peroxide generation, artificial photosynthesis, selective benzylamine oxidation, defective ZrS₃ nanobelts

Posted Date: September 21st, 2020

DOI: <https://doi.org/10.21203/rs.3.rs-73943/v1>

License:  This work is licensed under a Creative Commons Attribution 4.0 International License.

[Read Full License](#)

Version of Record: A version of this preprint was published at Nature Communications on April 1st, 2021. See the published version at <https://doi.org/10.1038/s41467-021-22394-8>.

Abstract

Photocatalytic hydrogen peroxide (H_2O_2) generation represents a promising approach for artificial photosynthesis. However, the sluggish half-reaction of water oxidation significantly limits the efficiency of H_2O_2 generation. A substitutional reaction of oxidation with accelerated kinetics to produce value-added chemicals holds promise to tackle this challenge. Here, a benzylamine oxidation with more favorable thermodynamics is employed as the half-reaction to couple with H_2O_2 generation in water by using defective zirconium trisulfide (ZrS_3) nanobelts as photocatalyst. The ZrS_3 nanobelts with disulfide (S_2^{2-}) and sulfide anion (S^{2-}) vacancies exhibit an excellent photocatalytic performance for H_2O_2 generation and simultaneous oxidation of benzylamine to benzonitrile with a high selectivity of >99%. The S_2^{2-} vacancies are revealed to facilitate the separation of photogenerated charge carriers. The S^{2-} vacancies can significantly improve the electron conduction, hole extraction, and kinetics of benzylamine oxidation. As a result, the use of defective ZrS_3 nanobelts yields a high production rate of 78 and 32 $\mu\text{mol h}^{-1}$ for H_2O_2 and benzonitrile, respectively, under a simulated sunlight irradiation.

Introduction

Artificial photosynthesis, i. e. the conversion of solar energy into chemical energy, is considered as one of the promising approaches to synthesize chemicals with the unlimited energy source and minimized environmental problems.^{1,2} As a novel liquid solar fuel generated by artificial photosynthesis, hydrogen peroxide (H_2O_2) has attracted growing attention because of its high commercial value and low transportation cost.³ Substantial efforts have been devoted to the development of effective photocatalysts for the H_2O_2 generation from water and O_2 .⁴ In this photocatalytic process, the sluggish oxidation of water induced by the photogenerated valence holes is a limiting factor for the production of H_2O_2 .⁵⁻⁹ Most previous reports focused on improving the half-reaction of O_2 reduction, e. g. by consuming holes with sacrificial agents, such as isopropyl alcohol, benzyl alcohol, and 2-PrOH.^{3,10,11} However, the development of an alternative oxidation reaction with accelerated kinetics to produce value-added chemicals was rarely reported. On the other hand, selective oxidation of amines to nitriles with lower oxidation potential than water plays an vital role in both laboratorial and industrial synthetic process since nitriles are the important intermediates during the synthesis of fine chemicals, pharmaceuticals, and agrochemicals.¹²⁻¹⁹ Intensive research has been carried out to synthesize nitriles from primary nitriles through dehydrogenation.²⁰⁻²⁵ However, most of the reactions are conducted in organic solvents under harsh conditions, such as high-temperature, exposure to high-pressure oxygen or air, and presence of oxidants. Thus, the development of artificial photosynthesis with appropriate photocatalysts for such reactions is highly desirable for the production of nitriles in an economically-viable and environment-friendly way.

Monoclinic zirconium trisulfide (ZrS_3) (ICCD PDF no. 30-1498), a layered n-type transition metal trichalcogenide (TMT), has recently drawn great research interest due to the extraordinary properties

arising from its unique disulfide anions (S_2^{2-}).²⁶ ZrS_3 has shown a good optical responsivity of 290 mA W^{-1} with an in-plane hole and electron mobility at a magnitude of 10^2 and $10^3 \text{ cm}^2 \text{ V}^{-1} \text{ s}^{-1}$, respectively.²⁷⁻³⁰ In particular, ZrS_3 possesses a bandgap of $\sim 2 \text{ eV}$ with a more negative conduction band minimum (CBM) than the H_2 evolution potential,³¹ making ZrS_3 a promising semiconductor for photocatalytic and photoelectrochemical applications. The previous studies on zirconium nitride have demonstrated that its superior performance for O_2 reduction stems from the interaction between Zr sites and oxide species, where the Zr d-orbitals make a strong contribution.³² Intriguingly, the conduction band of ZrS_3 is mainly composed of Zr d-orbitals,^{27,29} which has a much more negative potential than the reducing potential of O_2 to H_2O_2 . Therefore, ZrS_3 shows great potential for the photocatalytic H_2O_2 generation.

There are three categories of S (S_1 , S_2 , and S_3) environments in monoclinic ZrS_3 lattice, where S_1 denotes the sulfide ion (S^{2-}) and S_2 , S_3 are interpreted as the S_2^{2-} (**Schematic 1a and b**).³³ Recently, both theoretical calculations and experimental investigations have demonstrated that moderate S_2^{2-} vacancies can greatly promote the separation of photogenerated charge carriers in TMTs (**Schematic S1a and b**).^{34,35} In addition, the anion vacancies existing on the surface of n-type semiconductors can further improve its photocatalytic and photoelectrochemical performance by accelerating the kinetics of hole transfer on the surface.³⁶⁻³⁹ The crystal structure analysis of ZrS_3 inspires us that the S_2^{2-} and S^{2-} vacancies can be separately introduced into ZrS_3 by different methods (**Schematic 1 and S1**).

Experimentally, hexagonal ZrS_2 (ICCD PDF no. 11-0679) is usually obtained by vacuum annealing of monoclinic ZrS_3 at elevated temperatures.⁴⁰ Only one type of Zr (Zr_1) and S (S_1) environment exists in ZrS_2 , where the Zr_1 - S_1 bond length is similar to that in ZrS_3 (**Schematic 1a-c**). Besides, ZrS_2 shows a similar layered structure to ZrS_3 , and atomic layers in both materials are parallel to the (001) plane (**Schematic S1c-f**). When ZrS_3 transforms into ZrS_2 , it does not need much tweaking of the framework along both [010] and [001] directions (**Schematic S1c and e**), but it is required to adjust the framework along the [100] direction (**Schematic 1d and f**). **Schematic 1** clearly suggests that the ZrS_3 can transform into ZrS_2 by two steps: the first step can be the desulfurization of ZrS_3 to release S_2 or S_3 ions to form a distorted crystal structure of ZrS_2 (**Schematic 1a, b, d and e**), and then the distorted crystal structure undergoes structural relaxation by tuning the length and angle of Zr-S bonds to form ZrS_2 without breaking or regrouping the bonds (**Schematic 1b, c, e and f**). Thus, the high-temperature vacuum annealing is expected to be an effective scheme to produce S_2^{2-} vacancies in ZrS_3 . On the other hand, S^{2-} ions have the high adaptability when coordinated with metal ions, which can serve as either terminal or bridge ions to interact with metals (especially for alkali metals). This is different with the S_x^{2-} ($x \geq 2$) ions that are difficult to bond with metals (**Schematic S1g**).⁴¹ Moreover, ZrS_3 is easily formed as nanobelts (NBs) with rich S^{2-} ions exposed at the edges (**Schematic 1h and i**). As a typical alkali metal with high reducibility, Li has been widely utilized to prepare superconducting materials and induce vacancies.⁴²⁻⁴⁵ Therefore, such Li-based treatment could be an effective approach to induce S^{2-} vacancies on ZrS_3 .

Here, ZrS₃ NBs with both S₂²⁻ and S²⁻ vacancies are employed to enhance the photocatalytic production of H₂O₂ coupled with the selective oxidation of benzylamine to benzonitrile (BN) in water. The impacts of S₂²⁻ and S²⁻ vacancies on modulating the charge carrier dynamics and photocatalytic performance are systematically investigated. The S₂²⁻ vacancies can significantly facilitate the separation of photogenerated charge carriers; while the S²⁻ vacancies are demonstrated to not only promote the electron conduction and hole extraction in photocatalytic process but also improve the kinetics of benzylamine oxidation. As a result, the use of defective ZrS₃ NBs as photocatalyst produces H₂O₂ and BN at a high rate of 78 and 32 μmol h⁻¹ respectively, under the illumination of a simulated sunlight.

Results

Synthesis and band structures of photocatalysts. ZrS₃ NBs were synthesized via a chemical vapor transport of S powder to Zr powder using iodine as a transport agent. ZrS₃ with S₂²⁻ vacancies (ZrSS_{2-x}) was obtained by the re-annealing of the as-grown ZrS₃ NBs at 700 °C for 15 min under vacuum. ZrSS_{2-x} with S²⁻ vacancies (ZrS_{1-y}S_{2-x}) was prepared through a low-temperature solvothermal treatment by using Li-dissolved ethanediamine. The x-ray diffraction (XRD) pattern indicates the formation of ZrS₃ in the monoclinic phase (ICCD PDF no. 30-1498), and the vacuum annealing and further Li treatment did not induce any phase transition in ZrSS_{2-x} and ZrS_{1-y}S_{2-x} NBs (**Figure S1**). The obtained ZrS₃ was formed as NBs with the width ranging from 400 nm to 3 μm and length in tens of micrometers (**Figure 1a-c**). The individual ZrS₃ NB is confirmed as the single crystal along [010] direction by the transmission electron microscopy (TEM) and corresponding selected area electron diffraction (SAED) characterization (**Figure 1d**). It is demonstrated that the ZrS₃ layer is parallel to the axial direction of NB, which is in favor of charge carrier transport.³⁴ As shown in the diffuse reflectance UV-vis spectra (**Figure 1e**), both ZrS₃ and ZrSS_{2-x} NBs absorb light with the wavelength up to ~650 nm, corresponding to a bandgap of 2.02 eV (**Figure S2**). ZrS_{1-y}S_{2-x} NBs present a slight red-shift of absorption spectrum, revealing a smaller bandgap of 1.98 eV. The Mott-Schottky plots for all three samples exhibit positive slopes, indicating the n-type behavior of ZrS₃ (**Figure 1f**). The flat band potentials (E_{fb}) of ZrS₃, ZrSS_{2-x}, and ZrS_{1-y}S_{2-x} are estimated to be -0.10, -0.11, and -0.18 V *versus* reversible hydrogen electrode (V_{RHE}), respectively (**Figure 1g and S3**). E_{fb} is commonly used to estimate the CBM for a series of n-type semiconductors at the surface in an aqueous environment, which agreed with their theoretically determined values.^{1,38,46-48} Previous studies on the energy positions of semiconductors have shown that the CBM of zirconium-based sulfides is very close to their E_{fb} ,^{31,47} and therefore the CBM of ZrS₃, ZrSS_{2-x}, and ZrS_{1-y}S_{2-x} can be directly determined by their E_{fb} . Based on the Mott-Schottky (**Figure 1f, g and S3**) and UV-vis spectra results, the CBM and valence band maximum (VBM) for ZrS₃, ZrSS_{2-x}, and ZrS_{1-y}S_{2-x} were revealed to be -0.10, -0.11, -0.18 V_{RHE} (CBM) and 1.92, 1.91, and 1.80 V_{RHE} (VBM), respectively (**Figure 1h and S4**). The CBMs of ZrS₃, ZrSS_{2-x}, and ZrS_{1-y}S_{2-x} are higher than the potential for two-electron reduction of O₂, and their VBMs lie far

below the oxidation potential of benzylamine,^{12,15,48,49} indicating that these photocatalysts are applicable to the photocatalytic O₂ reduction and benzylamine oxidation.

Characterizations of vacancy structure. Four characteristic Raman modes of ZrS₃ located at ~ 147, 274, 315, and 524 cm⁻¹ were observed in **Figure 2a**, which are assigned to the rigid chain vibration (I: A_g^{rigid}), internal out-of-plane vibrations (II: A_g^{internal} and III: A_g^{internal}), and S–S diatomic motion (IV: A_g^{s-s}), respectively.²⁹ The Raman spectra show an obvious red-shift of A_g^{s-s} mode by ~5 cm⁻¹ from ZrS₃ to ZrSS_{2-x} and ZrS_{1-y}S_{2-x}, originating from the introduction of S₂²⁻ vacancies.³⁴ We also observed a 3 cm⁻¹ red-shift of A_g^{rigid} mode from ZrS₃ and ZrSS_{2-x} to ZrS_{1-y}S_{2-x}. Since the A_g^{rigid} is correlated to the vibration of quasi-one-dimensional chains in the direction of c axis (**Figure S5a**), the shift of A_g^{rigid} mode in ZrS_{1-y}S_{2-x} results from the introduction of S²⁻ vacancies, which alters the length of Zr–S bonds within each chain. The similar shift of A_g^{rigid} mode was also identified from ZrS₃ and ZrSS_{2-x} to the only Li-treated ZrS₃ (ZrS_{1-y}S) (**Figure S5b**). The XPS characterization was conducted on these samples to further confirm the vacancy type. After the vacuum annealing, the ZrSS_{2-x} NBs exhibit a slightly higher binding energy of the Zr 3d core level than ZrS₃ NBs, consistent with the results from ZrS₃ to ZrS₂ (**Figure S6a**).⁵⁰ Furthermore, ZrSS_{2-x} shows a significant attenuation of S₂²⁻ 2p peaks with the nearly unchanged S²⁻ 2p peaks compared to ZrS₃ (**Figure 2b and S6b**), indicating the mere increase of S₂²⁻ vacancies in ZrSS_{2-x}. After further Li treatment, both Zr 3d and S 2p core levels of ZrS_{1-y}S_{2-x} NBs apparently shifted to the higher binding energy by ~0.3 eV with reference to ZrSS_{2-x} (**Figure S6a and b**) due to the increased electron densities around the Zr sites induced by the S²⁻ vacancies.⁵¹ In particular, the intensity of S²⁻ 2p peaks in the ZrS_{1-y}S_{2-x} was clearly lower than that of ZrSS_{2-x} (**Figure 2b and S6b**), revealing the increase of S²⁻ vacancies. The similar variation of Zr 3d and S 2p spectra observed from ZrS₃ to ZrS_{1-y}S further suggest the separate introduction of S²⁻ vacancies by the Li treatment (**Figure S6a and b**). In addition, the electron paramagnetic resonances (EPR) investigation was also carried out to detect the vacancy structure. Both ZrS_{1-y}S_{2-x} and ZrSS_{2-x} NBs show a similar characteristic peak located at g = 2.004, suggesting the formation of sulfur vacancies.⁵² The higher signal intensity of ZrS_{1-y}S_{2-x} than that of ZrSS_{2-x} indicates more sulfur vacancies existing in ZrS_{1-y}S_{2-x} NBs. In order to have a direct view of the atomic arrangement for ZrSS_{2-x} and ZrS_{1-y}S_{2-x} NBs, the high-angle annular dark-field scanning transmission electron microscopy (HAADF-STEM) images were obtained, where the atomic sites can be determined by comparing the HAADF-STEM image with the crystal structure of ZrS₃ lattice along the [001] direction (**Figure S5c and d**). The ZrSS_{2-x} demonstrates the missing atoms only emerging on the S₂²⁻ sites, as indicated by the red dashed circles in **Figure 2d**, while the atomic vacancies exist on both S²⁻ (indicated by yellow dashed circles) and S₂²⁻ sites for ZrS_{1-y}S_{2-x} (**Figure 2e**).

Photocatalytic performance. The photocatalytic capability of the defective ZrS₃ NBs for reducing O₂ to create the reactive oxygen species (ROS) was first evaluated by the EPR trapping experiment using 5,5-dimethyl-1-pyrroline N-oxide (DMPO). As illustrated in **Figure 3a**, four characteristic peaks of DMPO–O₂^{•-}

were observed for all NBs, confirming the generation of $O_2^{\cdot-}$.⁵²⁻⁵⁴ The introduction of S_2^{2-} vacancies was found to enhance the reduction of O_2 to $O_2^{\cdot-}$, and the additional introduction of S^{2-} vacancies led to a further increased photocatalytic activity. Thus, $ZrS_{1-y}S_{2-x}$ NBs possess a high H_2O_2 evolution rate of $90 \mu\text{mol h}^{-1}$ with the presence of benzyl alcohol as the hole scavenger (entry 5 in **Table S1**), which is higher than most previous reports (**Table S2**). The wavelength-dependent apparent quantum yield (AQY) for the H_2O_2 generation on $ZrS_{1-y}S_{2-x}$ agrees well with its absorption spectrum, revealing that the photocatalytic activity originates from the bandgap excitation of $ZrS_{1-y}S_{2-x}$ (**Figure 3b**). In particular, $ZrS_{1-y}S_{2-x}$ produces an AQY of 11.4 and 10.8 % for the incident light of 400 and 500 nm respectively, and demonstrates a good activity even with the excitation extended to the near-infrared region of ~ 700 nm. Furthermore, the photocatalyst of $ZrS_{1-y}S_{2-x}$ is able to maintain its activities after being recycled for the same reaction, as presented in **Figure 3c**. Based on the high activity of $ZrS_{1-y}S_{2-x}$ for H_2O_2 generation, we further utilized benzylamine to substitute the hole scavenger. The H_2O_2 evolution rate of $ZrS_{1-y}S_{2-x}$ was decreased to $78 \mu\text{mol h}^{-1}$ with the same molar amount of benzylamine as benzyl alcohol, due to the slower oxidation kinetics of benzylamine than that of benzyl alcohol. Simultaneously, the benzylamine was oxidized and converted to BN at a rate of $32 \mu\text{mol h}^{-1}$ with a high selectivity of $> 99\%$ (entry 2 in **Table S1** and **Figure 3d**). Similar photocatalytic behaviors were also identified on both $ZrSS_{2-x}$ and ZrS_3 NBs, which produced the H_2O_2 at a rate of 58 and $30 \mu\text{mol h}^{-1}$ with the hole scavenger (entry 3 and 1 in **Table S1**), respectively. As a comparison, $ZrSS_{2-x}$ and ZrS_3 show a decreased H_2O_2 evolution rate of 48 and $18 \mu\text{mol h}^{-1}$ with the use of benzylamine, and the corresponding BN generation rates are 21 and $7 \mu\text{mol h}^{-1}$, respectively (**Figure 3d**). As a result, the comparison of photocatalytic performance among $ZrS_{1-y}S_{2-x}$, $ZrSS_{2-x}$, and ZrS_3 reveals the key role of S_2^{2-} and S^{2-} vacancies on the O_2 reduction and benzylamine oxidation.

To provide a deep insight into the effect of defective structures in ZrS_3 NBs on its photocatalytic performance, the transient open-circuit potential measurements were performed on ZrS_3 , $ZrSS_{2-x}$, and $ZrS_{1-y}S_{2-x}$ NBs to reveal the lifetime of photo-induced charge carriers (**Figure S7** and **Equation S3**). After introducing S_2^{2-} vacancies, the carrier lifetime of $ZrSS_{2-x}$ was significantly increased to 0.69 s as compared to 0.3 s of ZrS_3 , while the $ZrS_{1-y}S_{2-x}$ exhibits a further enhanced lifetime of 0.82 s, as shown in **Figure 4a**. The increased photocurrent for the defective ZrS_3 also suggests the role of S_2^{2-} and S^{2-} vacancies on improving the carrier lifetime and dynamics (**Figure S8**). In order to explore the underlying mechanism for the lifetime enhancement, the charge carrier dynamics of these samples were extracted through the Mott–Schottky method. According to the Mott–Schottky equation (**Equation S1**), the electron concentrations of ZrS_3 , $ZrSS_{2-x}$, and $ZrS_{1-y}S_{2-x}$ NBs were calculated to be 4.00×10^{18} , 5.35×10^{18} and $4.58 \times 10^{19} \text{ cm}^{-3}$, based on the estimated width of the depletion region (w_d) under the illumination of 55, 46, and 17 nm, respectively (**Equation S2**). The similar band bending between ZrS_3 and $ZrSS_{2-x}$ suggests that the significantly enhanced carrier lifetime in $ZrSS_{2-x}$ is attributed to the role of S_2^{2-} vacancies in reducing electron-hole recombination rather than band bending, in agreement with the previous theoretical calculation.³⁵ The significantly reduced w_d in $ZrS_{1-y}S_{2-x}$ indicates a large electric field strength

on the surface of $\text{ZrS}_{1-y}\text{S}_{2-x}$, which can accelerate the extraction of photogenerated holes towards the surface and limit the internal band-to-band recombination. Moreover, the small w_d in $\text{ZrS}_{1-y}\text{S}_{2-x}$ results in a large conduction region for the free electrons compared to ZrS_3 and ZrSS_{2-x} , which is beneficial for the electron transport. On the other hand, the reaction kinetics of benzylamine oxidation on the photocatalysts were also investigated by the intensity-modulated photocurrent spectroscopy (IMPS). The typical IMPS plots are shown in **Figure S9**, and the details for the calculation of rate constant of charge transfer (k_t) and surface recombination (k_{rec}) are discussed in the supporting information. The higher $k_t/(k_t + k_{\text{rec}})$ of ZrSS_{2-x} and $\text{ZrS}_{1-y}\text{S}_{2-x}$ than that of ZrS_3 indicates a more efficient benzylamine oxidation for the defective ZrS_3 (**Figure 4b**).³⁷ The ZrSS_{2-x} exhibits a decreased k_{rec} compared to ZrS_3 (**Figure 4c and d**), revealing that the more efficient benzylamine oxidation on ZrSS_{2-x} stems from the enhanced carrier lifetime induced by the S_2^{2-} vacancies. The k_{rec} of $\text{ZrS}_{1-y}\text{S}_{2-x}$ was further decreased due to its efficient hole extraction induced by the large surface band bending. Furthermore, the increase of k_t for $\text{ZrS}_{1-y}\text{S}_{2-x}$ compared to ZrSS_{2-x} suggests that the S^{2-} vacancies can act as an additional photocatalytic layer for the benzylamine oxidation (**Figure 4d**).

Conclusions

In summary, we have developed an efficient photocatalyst of $\text{ZrS}_{1-y}\text{S}_{2-x}$ NBs with S_2^{2-} and S^{2-} vacancies for the integration of photocatalytic H_2O_2 generation with the selective oxidation of benzylamine to BN in water. The unique S_2^{2-} vacancies and S^{2-} vacancies in $\text{ZrS}_{1-y}\text{S}_{2-x}$ are induced separately by the vacuum annealing and Li-treatment, respectively. With the introduction of S_2^{2-} vacancies, the charge carrier recombination is prominently suppressed, and the surface S^{2-} vacancies are revealed to improve the electron conduction, surface hole extraction, and kinetics of benzylamine oxidation. As a result, the photocatalyst of $\text{ZrS}_{1-y}\text{S}_{2-x}$ exhibits a high generation rate of 78 and 32 $\mu\text{mol h}^{-1}$ for H_2O_2 and BN, respectively. Furthermore, $\text{ZrS}_{1-y}\text{S}_{2-x}$ NBs possesses a photoexcitation up to ~ 700 nm and delivers a high AQY of 11.4 and 10.8% under the incident light of 400 and 500 nm, respectively. Our results promise a novel strategy for the artificial photosynthesis of liquid solar fuels and other valuable chemicals.

Methods

Preparation of ZrS_3 , ZrSS_{2-x} and $\text{ZrS}_{1-y}\text{S}_{2-x}$ NBs: The ZrS_3 NBs were synthesized through a typical chemical vapor transport process. S (99.5 % purity, Alfa Aesar) and Zr (99.2 % purity, Sigma-Aldrich) powders were mixed according to a molar ratio of 1:3, and 5mg iodine (99.5 % purity, Alfa Aesar) was added as a transport agent. The mixture was sealed in a quartz ampoule (Φ 6 mm \times 200 mm) under the vacuum of 10^{-3} Pa, which was subsequently placed in the centre of a two-zone furnace with a temperature gradient of ca. 15 K/cm from center to edge. The furnace was heated to 650 $^\circ\text{C}$ and last for 10 h to produce ZrS_3 powder. The obtained ZrS_3 powder was then dispersed in isopropanol (≥ 99.5 % purity, Alfa Aesar) at a concentration of 0.5 mg ml^{-1} followed by the sonication for 15 min. The dispersion

was subsequently centrifuged for 10 min at 3000 rpm to remove large aggregates. Finally, the ZrS_3 NBs were obtained by the collection from the rest of dispersion.

The ZrSS_{2-x} NBs were prepared using the previously reported vacuum annealing method.³⁴ Specifically, the as-grown ZrS_3 NBs were sealed in the quartz ampule again, which was then heated to 700 °C and last for 15 mins to fabricate ZrSS_{2-x} NBs. In addition, 0.5 g ZrSS_{2-x} NBs were placed in a 50 mL Teflon-lined autoclave filled with 30 mL ethanediamine (≥ 98 % purity, Sigma-Aldrich) and 100 mg Li, and the autoclave was subsequently kept in an oven at 120 °C for 24 h. After cooling down to the room temperature, the mixture was first washed in 0.2 M HCl and then rinsed several times in deionized water and ethanol, where the $\text{ZrS}_{1-y}\text{S}_{2-x}$ NBs was finally obtained.

Characterization of photocatalysts: UV-Vis-NIR spectrometer (Hitachi U4100), field emission SEM (FE-SEM, JEOL JSM6700F), TEM (FEI Titan 80-300, operated at 200 kV), XRD (Bruker D8 Advance), XPS (ESCALAB 250Xi) with Al $K\alpha$ X-ray as the excitation source, EPR (JEOL FA200) and Raman spectroscopy (Horiba Jobin Yvon Modular Raman Spectrometer) with 514 nm laser excitation were employed to characterize different properties of the defective ZrS_3 NBs, e. g. atomic and energy band structure. In particular, the samples for the TEM measurements were suspended in ethanol and supported onto a holey carbon film on a Cu grid.

Coupling photocatalytic H_2O_2 generation with selective benzylamine oxidation over ZrS_3 , ZrSS_{2-x} , $\text{ZrS}_{1-y}\text{S}_{2-x}$ NBs: 50 mg photocatalyst was dispersed in 30 ml H_2O with 1 mmol benzylamine. After the sonication for a few seconds, the mixed solution was bubbled by oxygen for 30 s. Subsequently, the solution was sealed and irradiated under an AM 1.5G simulated sunlight of 100 mW cm^{-2} derived from a 300 W xenon lamp fitted with an AM 1.5 filter. At certain time intervals, the solution was filtrated by a 0.45 μm Millipore filter to remove the photocatalyst. The aqueous and organic phase products were then analyzed by the iodometry and gas chromatograph (GC) measurements, respectively.

The production of H_2O_2 was analyzed by the iodometry.¹⁰ Typically, 50 μL 0.4 M potassium iodide (KI, ≥ 99 % purity, Sigma-Aldrich) aqueous solution and 50 μL 0.1 M potassium hydrogen phthalate (≥ 99.5 % purity, Sigma-Aldrich) aqueous solution were added to 2ml obtained aqueous phase product, which was kept for 0.5h. The mixed solution was then detected by UV-vis spectroscopy on the basis of absorbance at 350 nm, from which the quantity of generated H_2O_2 was estimated. In addition, to analyze organic phase product from the benzylamine oxidation, the organic liquid was first extracted using ethyl acetate (≥ 99.9 % purity, Sigma-Aldrich) and then detected by the GC characterization.

Photocatalytic H_2O_2 generation with benzyl alcohol as hole sacrificial reagent: 50 mg catalyst was dispersed in 30 ml H_2O containing 1mmol benzyl alcohol. After sonicating for a few seconds, the mixed solution was bubbled by oxygen for 30 s. Subsequently, the solution was sealed and irradiated under an AM 1.5G simulated sunlight of 100 mW cm^{-2} derived from a 300 W xenon lamp fitted with an AM 1.5 filter. The amount of H_2O_2 was analyzed by the iodometry. For the action spectrum analysis, the reactions

were performed at 298 K under monochromated light irradiation, with the ϕ_{AQY} (AQY, apparent quantum yield) determined by the following equation (1):

$$\phi_{AQY}(\%) = \frac{[\text{H}_2\text{O}_2 \text{ formed (mol)}] \times 2}{[\text{photon number entered into the reactor (mol)}]} \times 100 \quad (1)$$

EPR Trapping Measurements: 4 mg catalyst was suspended in 500 μL CH_3OH containing 50 μL DMPO (Sigma-Aldrich for ESR-spectroscopy). After the sonication, the solution was irradiated by a 300 W xenon lamp with a 420 nm filter for 3 min. The resulted solution was subjected to the analysis by using a JEOL (FA200) ESR Spectrometer.

Photoelectrochemical measurement: The photoelectrochemical measurements were performed in a three-electrode system with an electrochemical workstation (Zahner Zennium) under an AM 1.5G simulated sunlight of 100 mW cm^{-2} (150 W, Newport 94011A LCS-100). Samples on FTO substrates were directly used as the working electrode, with a Pt wire and an Ag/AgCl (KCl saturated) electrode as counter and reference electrodes respectively. All the samples were illuminated through the sample side (front-side illumination). The photoelectrochemical performance was recorded in 0.1 M Na_2SO_4 electrolyte with 0.1 mM benzylamine. Mott-Schottky plots were derived from impedance-potential tests conducted at a frequency of 1 kHz in dark. IMPS spectra were recorded by the Zahner Zennium C-IMPS system.

Data availability

All data supporting the findings in the article as well as the Supplementary Information files are available from the corresponding authors on reasonable request.

Declarations

Acknowledgments

The authors acknowledge the financial support from Singapore National Research Foundation under the grant of NRF2017NRF-NSFC001-007, NUS Flagship Green Energy Programme, Fundamental Research Foundation of Shenzhen (No. JCYJ20190808152607389 and No. JCYJ20170817100405375), China Postdoctoral Science Foundation (2020M672794), and Shenzhen Peacock Plan (No. KQTD2016053112042971).

Author contributions

T.Z., H.C., L.H. and C.W. conceived and designed the experiments. T.Z., Z.Y., D.W., L.X., W.Y. and Z.Y. performed the experiments. T.Z., L.X. and H.Z. analyzed the data. T.Z., S.Y., and P.X. wrote the manuscript. All authors discussed the results and commented on the manuscript.

References

1. Shiraishi, Y. *et al.* Resorcinol–formaldehyde resins as metal-free semiconductor photocatalysts for solar-to-hydrogen peroxide energy conversion. *Nat. Mater.* **18**, 985–993 (2019).
2. Chen, S., Takata, T. & Domen, K. Particulate photocatalysts for overall water splitting. *Nat. Rev. Mater.* **2**, 1–17 (2017).
3. Kofuji, Y. *et al.* Hydrogen Peroxide Production on a Carbon Nitride–Boron Nitride-Reduced Graphene Oxide Hybrid Photocatalyst under Visible Light. *ChemCatChem* **10**, 2070–2077 (2018).
4. Hou, H., Zeng, X. & Zhang, X. Production of Hydrogen Peroxide by Photocatalytic Processes. *Angew. Chem. Int. Ed.* **59**, 2–23 (2020).
5. Teranishi, M., Naya, S.-i. & Tada, H. In situ liquid phase synthesis of hydrogen peroxide from molecular oxygen using gold nanoparticle-loaded titanium (IV) dioxide photocatalyst. *J. Am. Chem. Soc.* **132**, 7850–7851 (2010).
6. Kato, S., Jung, J., Suenobu, T. & Fukuzumi, S. Production of hydrogen peroxide as a sustainable solar fuel from water and dioxygen. *Energy Environ. Sci.* **6**, 3756–3764 (2013).
7. Moon, G.-h., Kim, W., Bokare, A. D., Sung, N.-e. & Choi, W. Solar production of H₂O₂ on reduced graphene oxide–TiO₂ hybrid photocatalysts consisting of earth-abundant elements only. *Energy Environ. Sci.* **7**, 4023–4028 (2014).
8. Isaka, Y., Oyama, K., Yamada, Y., Suenobu, T. & Fukuzumi, S. Photocatalytic production of hydrogen peroxide from water and dioxygen using cyano-bridged polynuclear transition metal complexes as water oxidation catalysts. *Catal. Sci. Technol.* **6**, 681–684 (2016).
9. Kim, H.-i., Kwon, O. S., Kim, S., Choi, W. & Kim, J.-H. Harnessing low energy photons (635 nm) for the production of H₂O₂ using upconversion nanohybrid photocatalysts. *Energy Environ. Sci.* **9**, 1063–1073 (2016).
10. Wei, Z. *et al.* Efficient visible-light-driven selective oxygen reduction to hydrogen peroxide by oxygen-enriched graphitic carbon nitride polymers. *Energy Environ. Sci.* **11**, 2581–2589 (2018).
11. Shiraishi, Y. *et al.* Selective Hydrogen Peroxide Formation by Titanium Dioxide Photocatalysis with Benzylic Alcohols and Molecular Oxygen in Water. *ACS Catal.* **3**, 2222–2227 (2013).
12. Huang, Y., Chong, X., Liu, C., Liang, Y. & Zhang, B. Boosting Hydrogen Production by Anodic Oxidation of Primary Amines over a NiSe Nanorod Electrode. *Angew. Chem., Int. Ed.* **57**, 13163–13166 (2018).
13. Martin, A. & Kalevaru, V. N. Heterogeneously Catalyzed Ammoxidation: A Valuable Tool for One-Step Synthesis of Nitriles. *ChemCatChem* **2**, 1504–1522 (2010).
14. Jagadeesh, R. V., Junge, H. & Beller, M. Green synthesis of nitriles using non-noble metal oxides-based nanocatalysts. *Nat. Commun.* **5**, 1–8 (2014).
15. Łuczak, T. Electrochemical behaviour of benzylamine, 2-phenylethylamine and 4-hydroxyphenylethylamine at gold. A comparative study. *J. Appl. Electrochem.* **38**, 43–50 (2007).
16. Fleming, F. F., Yao, L., Ravikumar, P., Funk, L. & Shook, B. C. Nitrile-containing pharmaceuticals: efficacious roles of the nitrile pharmacophore. *J. Med. Chem.* **53**, 7902–7917 (2010).

17. Wang, T. & Jiao, N. Direct approaches to nitriles via highly efficient nitrogenation strategy through C–H or C–C bond Cleavage. *Acc. Chem. Res.* **47**, 1137–1145 (2014).
18. Yan, G., Zhang, Y. & Wang, J. Recent advances in the synthesis of aryl nitrile compounds. *Adv. Synth. Catal.* **359**, 4068–4105 (2017).
19. Liu, R. Y., Bae, M. & Buchwald, S. L. Mechanistic insight facilitates discovery of a mild and efficient copper-catalyzed dehydration of primary amides to nitriles using hydrosilanes. *J. Am. Chem. Soc.* **140**, 1627–1631 (2018).
20. Dutta, I. *et al.* Double Dehydrogenation of Primary Amines to Nitriles by a Ruthenium Complex Featuring Pyrazole Functionality. *J. Am. Chem. Soc.* **140**, 8662–8666 (2018).
21. Kim, J. & Stahl, S. S. Cu/nitroxyl-catalyzed aerobic oxidation of primary amines into nitriles at room temperature. *ACS Catal.* **3**, 1652–1656 (2013).
22. Lambert, K. M. *et al.* Metal-Free Oxidation of Primary Amines to Nitriles through Coupled Catalytic Cycles. *Chem. Eur. J.* **22**, 5156–5159 (2016).
23. Lambert, K. M. *et al.* Catalytic, Metal-Free Oxidation of Primary Amines to Nitriles. *Org. Synth.* **95**, 60–79 (2018).
24. Tseng, K.-N. T., Rizzi, A. M. & Szymczak, N. K. Oxidant-free conversion of primary amines to nitriles. *J. Am. Chem. Soc.* **135**, 16352–16355 (2013).
25. Ovoshchnikov, D. S., Donoeva, B. G. & Golovko, V. B. Visible-light-driven aerobic oxidation of amines to nitriles over hydrous ruthenium oxide supported on TiO₂. *ACS Catal.* **5**, 34–38 (2015).
26. Wu, K. *et al.* Unusual lattice vibration characteristics in whiskers of the pseudo-one-dimensional titanium trisulfide TiS₃. *Nat. Commun* **7**, 12952 (2016).
27. Ahammed, R. *et al.* ZrS₃/MS₂ and ZrS₃/MXY (M Mo, W; X, Y S, Se, Te; X ≠ Y) type-II van der Waals hetero-bilayers: Prospective candidates in 2D excitonic solar cells. *Appl. Surf. Sci.* **499**, 143894 (2020).
28. Yi, H. *et al.* The electronic band structure of quasi-one-dimensional van der Waals semiconductors: the effective hole mass of ZrS₃ compared to TiS₃. *J. Phys. Condens. Matter* **32**, 29LT01 (2020).
29. Wang, X. *et al.* Highly Polarized Photoelectrical Response in vdW ZrS₃ Nanoribbons. *Adv. Electron. Mater.* **5**, 1900419 (2019).
30. Tao, Y. R., Wu, X. C. & Xiong, W. W. Flexible visible-light photodetectors with broad photoresponse based on ZrS₃ nanobelt films. *Small* **10**, 4905–4911 (2014).
31. Flores, E., Ares, J. R., Ferrer, I. J. & Sánchez, C. Synthesis and characterization of a family of layered trichalcogenides for assisted hydrogen photogeneration. *Phys. Status Solidi Rapid Res. Lett.* **10**, 802–806 (2016).
32. Yuan, Y. *et al.* Zirconium nitride catalysts surpass platinum for oxygen reduction. *Nat. Mater.* **19**, 282–286 (2020).
33. Endo, K., Ihara, H., Watanabe, K. & Gonda, S. I. XPS STUDY OF ONE-DIMENSIONAL COMPOUNDS - TiS₃. *J. Solid State Chem.* **44**, 268–272 (1982).

34. Tian, Z. *et al.* Enhanced Charge Carrier Lifetime of TiS_3 Photoanode by Introduction of S_2^{2-} Vacancies for Efficient Photoelectrochemical Hydrogen Evolution. *Adv. Funct. Mater.*, **30**, 2001286 (2020).
35. Wei, Y. Q., Zhou, Z. H. & Long, R. Defects Slow Down Nonradiative Electron-Hole Recombination in TiS_3 Nanoribbons: A Time-Domain Ab Initio Study. *J. Phys. Chem. Lett.* **8**, 4522–4529 (2017).
36. Tian, Z. *et al.* Hydrogen plasma reduced black TiO_2B nanowires for enhanced photoelectrochemical water-splitting. *J. Power Sources* **325**, 697–705, (2016).
37. Tian, Z. *et al.* Highly Conductive Cable-Like Bicomponent Titania Photoanode Approaching Limitation of Electron and Hole Collection. *Adv. Funct. Mater.*, **28**, 1803328 (2018).
38. Tian, Z. *et al.* Novel Black $\text{BiVO}_4/\text{TiO}_{2-x}$ Photoanode with Enhanced Photon Absorption and Charge Separation for Efficient and Stable Solar Water Splitting. *Adv. Energy Mater.* **9**, 1901287 (2019).
39. Zhang, K. *et al.* Overcoming Charge Collection Limitation at Solid/Liquid Interface by a Controllable Crystal Deficient Overlayer. *Adv. Energy Mater.* **7**, 1600923 (2017).
40. Li, L. *et al.* Electrical transport and high-performance photoconductivity in individual ZrS_2 nanobelts. *Adv. Mater.* **22**, 4151–4156 (2010).
41. KD
Ed
Kanatzidis, M. & Sutorik, A. (Karlin, KD, Ed, 1995).
42. Burrard-Lucas, M. *et al.* Enhancement of the superconducting transition temperature of FeSe by intercalation of a molecular spacer layer. *Nat. Mater.* **12**, 15–19 (2013).
43. Hatakeda, T., Noji, T., Kawamata, T., Kato, M. & Koike, Y. New Li-Ethylenediamine-Intercalated Superconductor $\text{Li}_x(\text{C}_2\text{H}_8\text{N}_2)_y\text{Fe}_{2-z}\text{Se}_2$ with $T_c = 45$ K. *J. Phys. Soc. Jpn.* **82**, 123705 (2013).
44. Scheidt, E.-W. *et al.* Superconductivity at $T_c = 44$ K in $\text{Li}_x\text{Fe}_2\text{Se}_2(\text{NH}_3)_y$. *Eur. Phys. J. E Soft Matter* **85**, 1–5 (2012).
45. Yin, G. *et al.* Hydrogenated Blue Titania for Efficient Solar to Chemical Conversions: Preparation, Characterization, and Reaction Mechanism of CO_2 Reduction. *ACS Catal.* **8**, 1009–1017 (2018).
46. Resasco, J. *et al.* $\text{TiO}_2/\text{BiVO}_4$ Nanowire Heterostructure Photoanodes Based on Type II Band Alignment. *ACS Cent. Sci.* **2**, 80–88 (2016).
47. Xu, Y. & Schoonen, M. A. The absolute energy positions of conduction and valence bands of selected semiconducting minerals. *Am. Mineral.* **85**, 543–556 (2000).
48. Wang, Q. *et al.* Oxysulfide photocatalyst for visible-light-driven overall water splitting. *Nat. Mater.* **18**, 827–832 (2019).
49. Liu, H., Xu, C., Li, D. & Jiang, H. L. Photocatalytic Hydrogen Production Coupled with Selective Benzylamine Oxidation over MOF Composites. *Angew. Chem. Int. Ed. Engl.* **57**, 5379–5383 (2018).
50. Jellinek, F., Pollak, R. & Shafer, M. X-ray photoelectron spectra and electronic structure of zirconium trisulfide and triselenide. *Mater. Res. Bull.* **9**, 845–856 (1974).

51. Wang, X. *et al.* Single-Atom Vacancy Defect to Trigger High-Efficiency Hydrogen Evolution of MoS₂. *J. Am. Chem. Soc.* **142**, 4298–4308 (2020).
52. Sun, X. *et al.* Enhanced Superoxide Generation on Defective Surfaces for Selective Photooxidation. *J. Am. Chem. Soc.* **141**, 3797–3801 (2019).
53. Song, H., Wei, L., Chen, C., Wen, C. & Han, F. Photocatalytic production of H₂O₂ and its in situ utilization over atomic-scale Au modified MoS₂ nanosheets. *J. Catal.* **376**, 198–208 (2019).
54. Lei, J. *et al.* Robust photocatalytic H₂O₂ production over inverse opal g-C₃N₄ with carbon vacancy under visible light. *ACS Sustain. Chem. Eng.* **7**, 16467–16473 (2019).

Figures

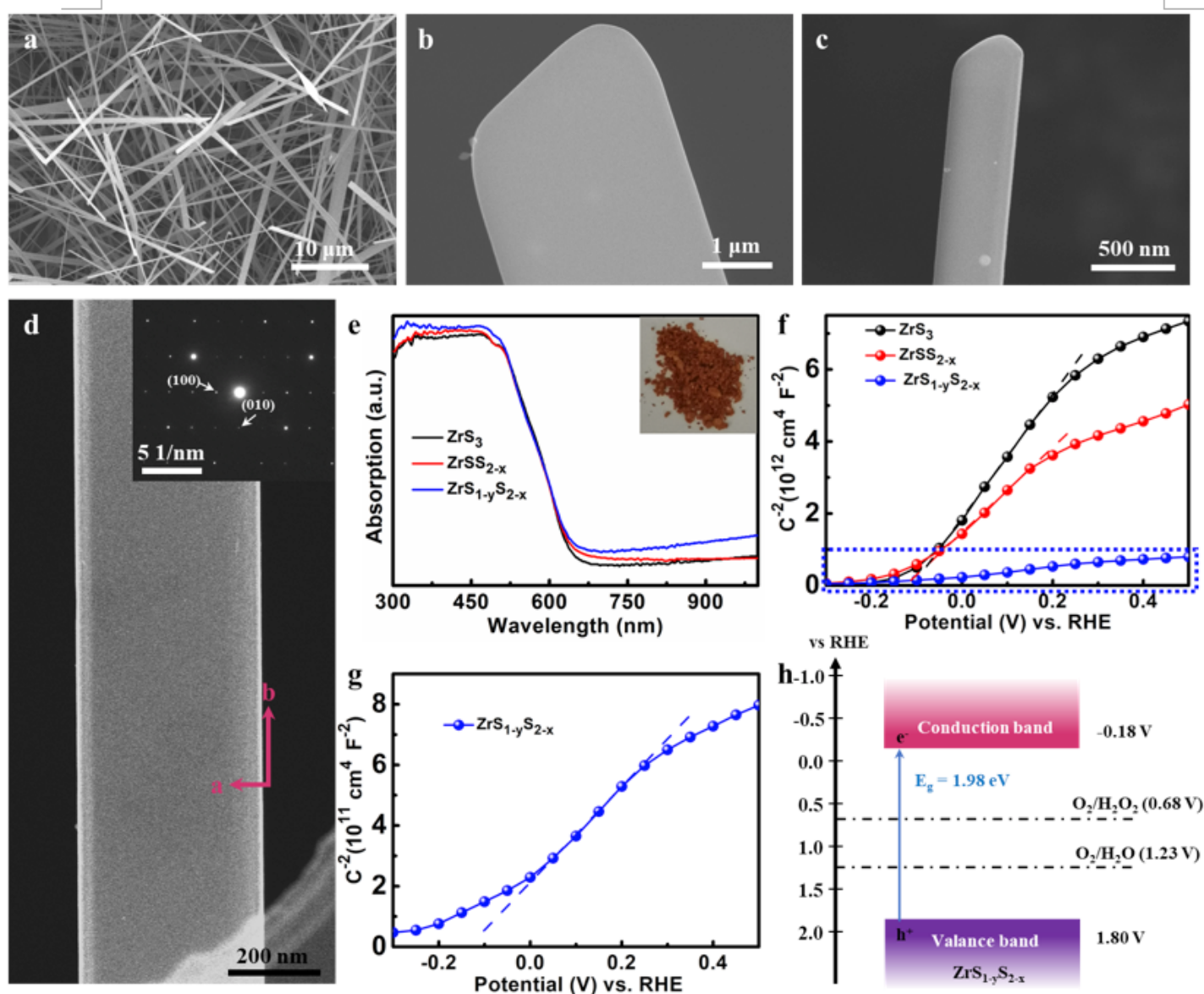


Figure 1

(a) Top-sectional, (b) and (c) high-magnification SEM images of the ZrS₃ NBs. (d) TEM image and SAED pattern of single ZrS₃ NB. (e) Diffuse reflectance UV–vis spectra of the ZrS₃, ZrSS_{2-x} and ZrS_{1-y}S_{2-x} NBs. Inset, photograph of the ZrS_{1-y}S_{2-x} NBs. (f) Mott–Schottky plots of ZrS₃, ZrSS_{2-x}, and ZrS_{1-y}S_{2-x} NBs. and (g) Mott-Schottky plot of ZrS_{1-y}S_{2-x} magnified from (f). (h) Schematic band structure diagram for ZrS_{1-y}S_{2-x}.

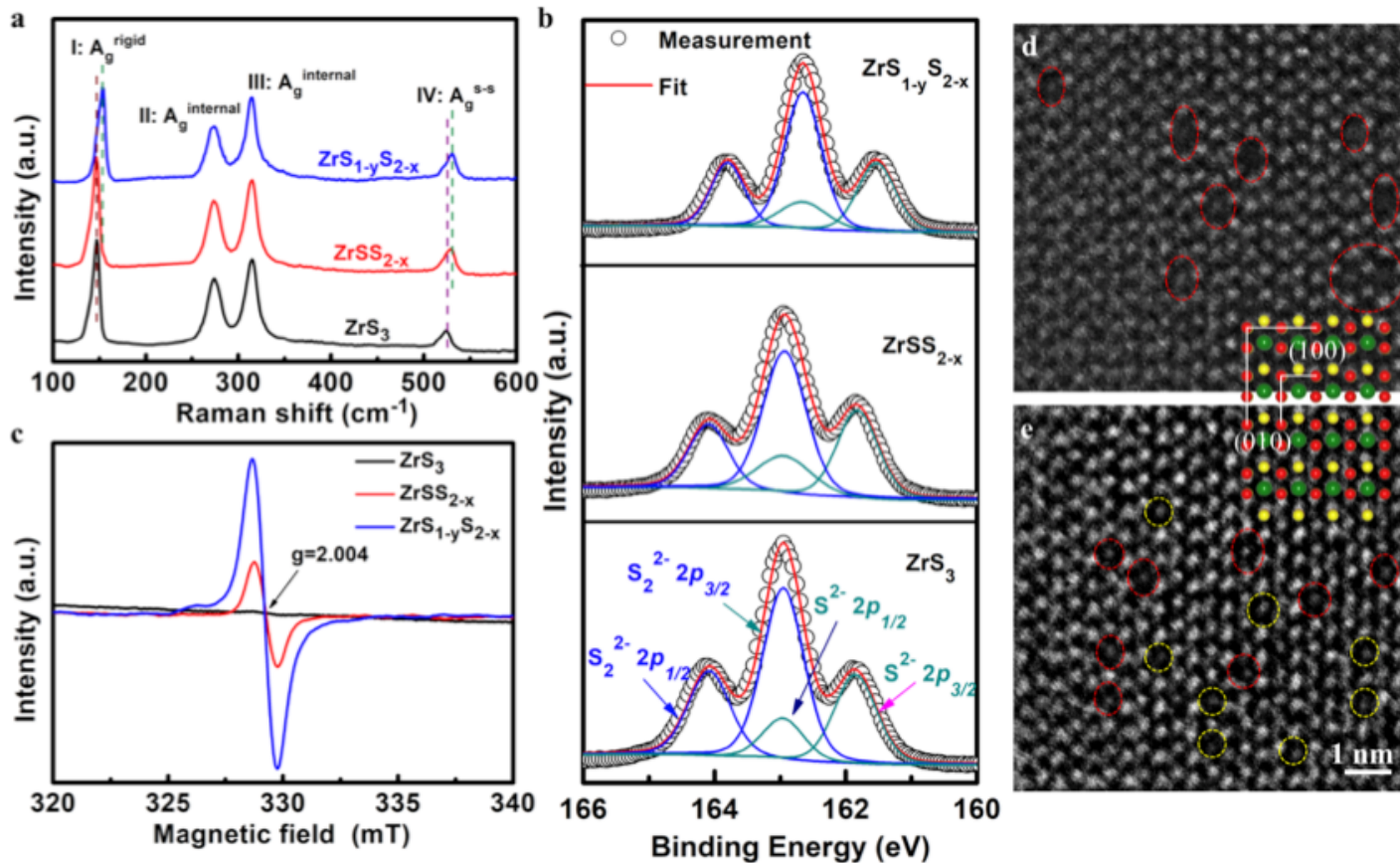


Figure 2

(a) Raman spectra, (b) S 2p XPS spectra, and (c) EPR spectra of the ZrS₃, ZrSS_{2-x} and ZrS_{1-y}S_{2-x} NBs. HAADF-STEM images of (d) ZrSS_{2-x} and (e) ZrS_{1-y}S_{2-x} measured from a spherical aberration-corrected TEM. Inset: the crystal lattice of ZrS₃ along the [001] orientation. The red and yellow circles represent S₂₂₋ and S₂₋, respectively.

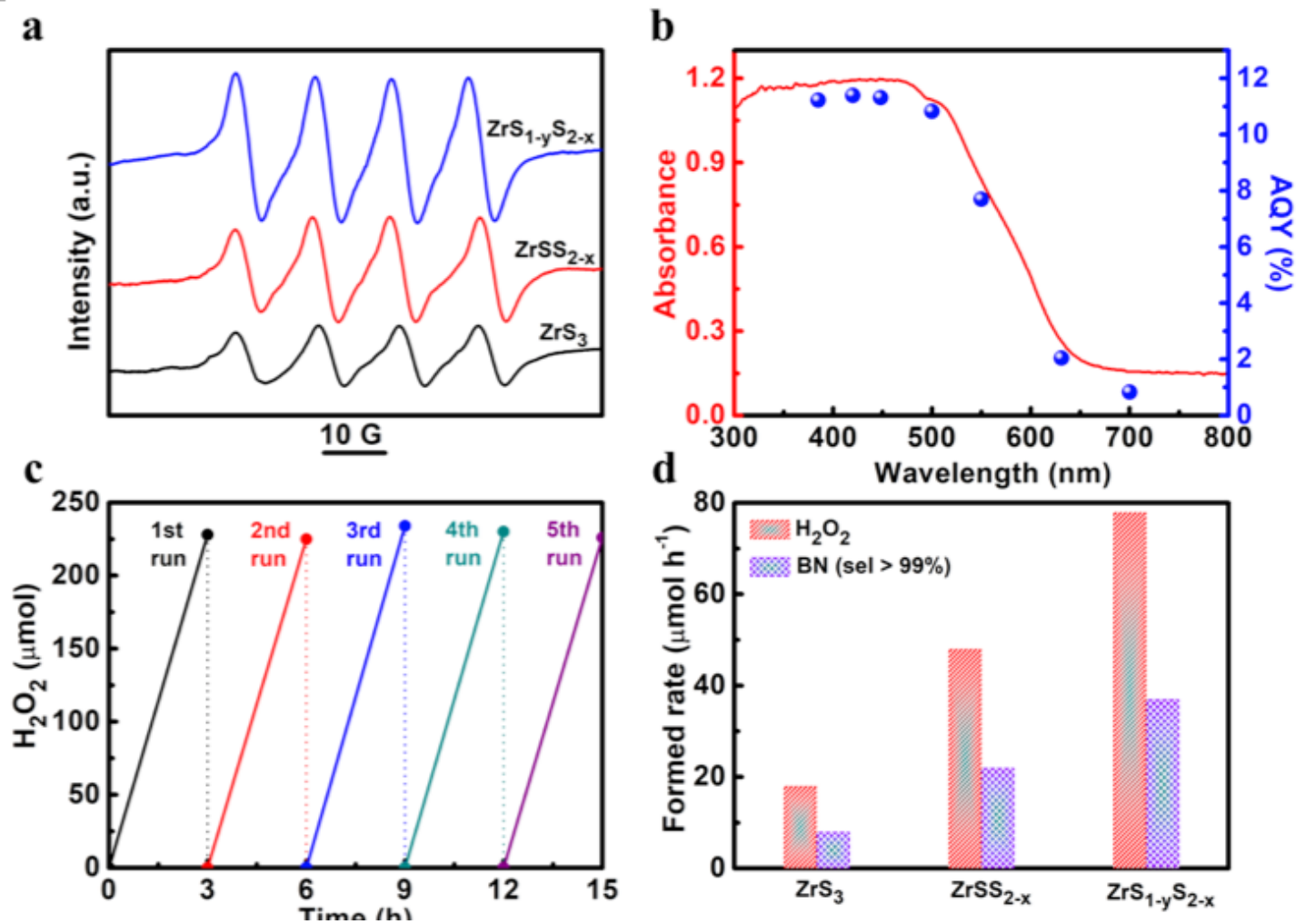


Figure 3

(a) EPR spectra of ZrS_3 , $ZrSS_{2-x}$ and $ZrS_{1-y}S_{2-x}$ in the presence of DMPO. (b) Absorption spectrum of $ZrS_{1-y}S_{2-x}$ and its dependence of AQY with monochromatic light irradiation. Conditions: 30 ml aqueous solution with 1 mmol benzyl alcohol, 50 mg photocatalysts. (c) Results for a repeated photoreaction sequence with $ZrS_{1-y}S_{2-x}$ under AM1.5G simulated sunlight irradiation. (d) H_2O_2 and BN evolution rate by the respective photocatalysts under AM1.5G simulated sunlight irradiation. Conditions: 30 ml H_2O with 1 mmol benzylamine, 50 mg photocatalysts, 1 bar O_2 .

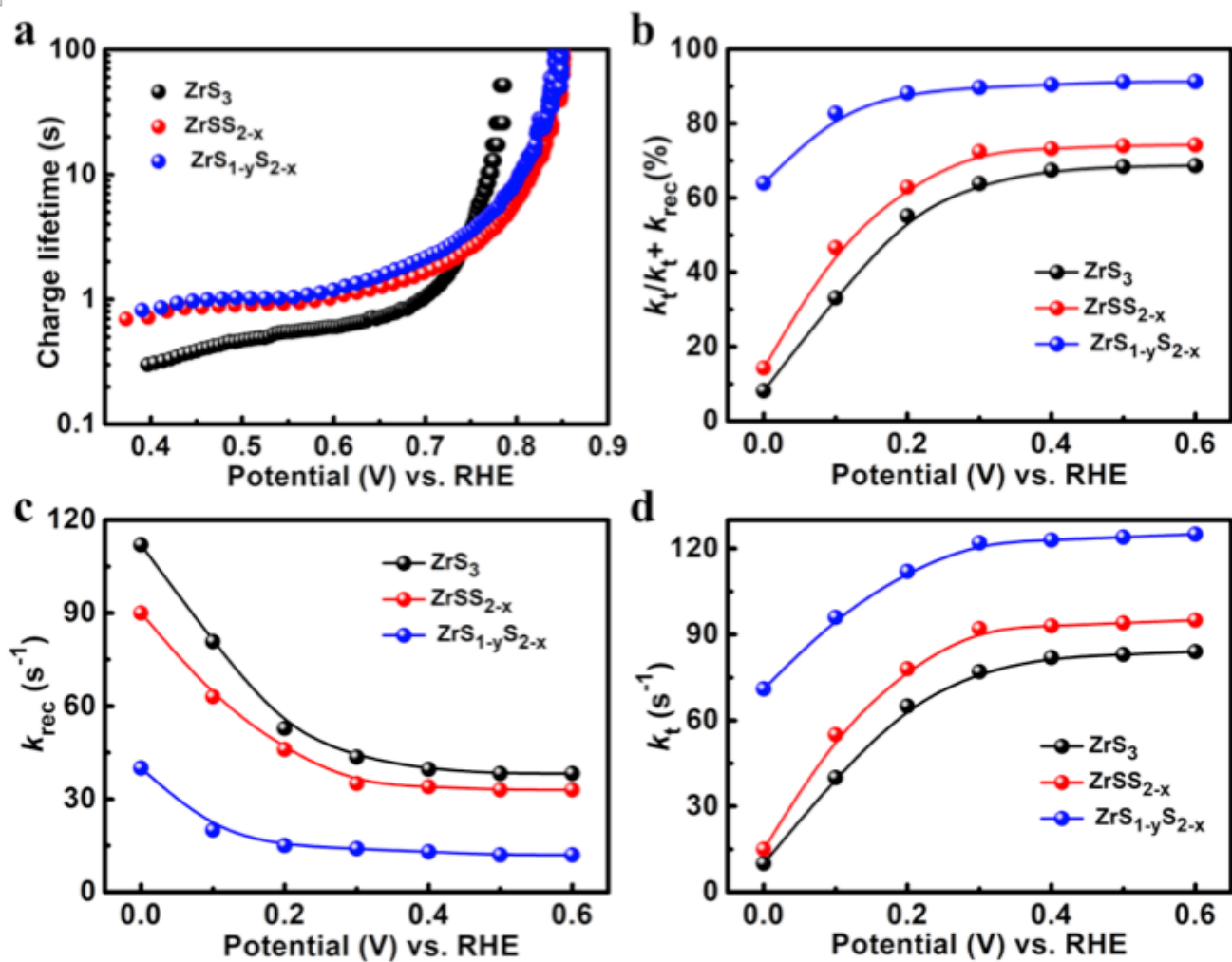


Figure 4

(a) The charge carrier lifetime of ZrS₃, ZrSS_{2-x} and ZrS_{1-y}S_{2-x} NBs. (b) Ratio of $k_t/(k_t + k_{rec})$, rate constants (c) k_t and (d) k_{rec} of ZrS₃, ZrSS_{2-x} and ZrS_{1-y}S_{2-x} for benzylamine oxidation measured in 0.5 M Na₂SO₄ with 0.1 M benzylamine.

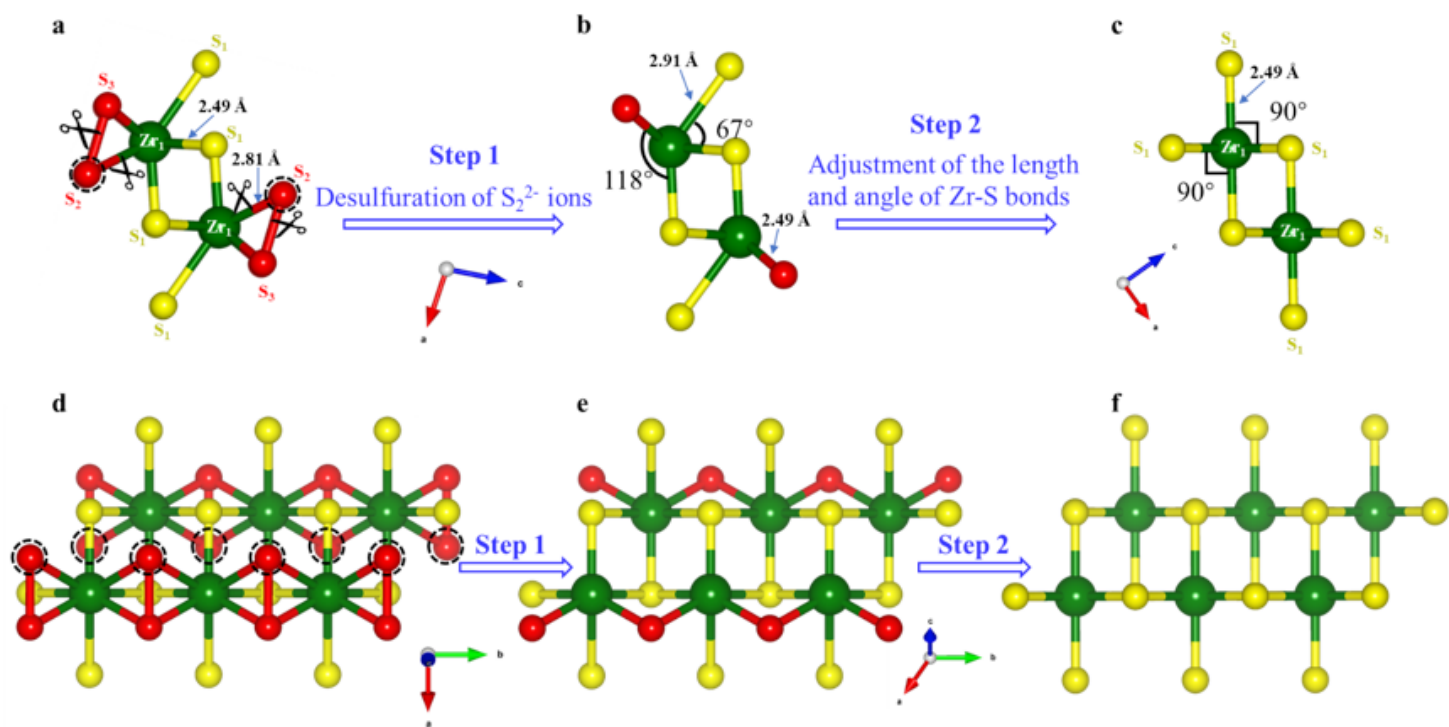


Figure 5

Schematic 1 The schematic process of the transformation of monoclinic ZrS₃ (ICCD PDF no. 30-1498) into hexagonal ZrS₂ (ICCD PDF no. 11-0679) from the [010] (a-c) and [001] (d-f) views. (a, d) Crystal structure of monolayer ZrS₃ with a boundary of from the [010] and [001] views, respectively. (b, e) Crystal structure of monolayer ZrS₃ after desulfuration of S₂²⁻ ions from (a) and (d), respectively. (c, f) Crystal structure of monolayer ZrS₂ with a boundary of from the [010] and [001] views, respectively.

Supplementary Files

This is a list of supplementary files associated with this preprint. Click to download.

- [SupportingXXInformation.docx](#)